

Electric-Field-Induced Instabilities in Thin Liquid Trilayers Confined between Patterned Electrodes

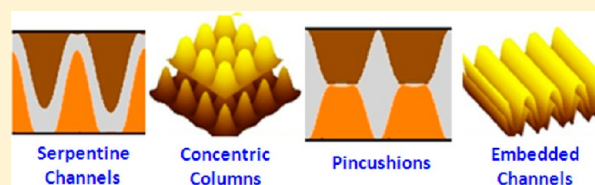
P. Dinesh Sankar Reddy,[†] Dipankar Bandyopadhyay,^{*,‡} and Ashutosh Sharma^{*,†}

[†]Department of Chemical Engineering, Indian Institute of Technology, Kanpur 208016, UP, India

[‡]Department of Chemical Engineering, Indian Institute of Technology, Guwahati 781039, Assam, India

S Supporting Information

ABSTRACT: Electric-field-induced instabilities of trilayer of immiscible thin films confined between both planar and patterned electrodes have been explored by the linear stability analysis (LSA) and the long-wave nonlinear simulations. The twin liquid–liquid interfaces of a trilayer can undergo either in-phase bending or antiphase squeezing or mixed modes of evolution. The linear and nonlinear analyses together uncover the conditions under which these modes evolve and subsequently form an array of interesting, complex patterns. The study confirms that when the middle layer is of the highest or lowest dielectric permittivity than the other layers the interfaces undergo a squeezing mode of deformation. In other cases, the interfaces evolve in the bending mode, except for the situations where the linear growth coefficient versus wavenumber curves in the LSA show a bimodal behavior and the interfaces evolve in a mixed mode. The LSA also highlights the importance of the ratios of the thermodynamic parameters such as thicknesses, dielectric permittivities, and interfacial tensions of the films in altering the length and time scales. Importantly, variation in the kinetic parameters such as the ratio of the viscosities of the films can also alter the modes of evolution, relative amplitudes of deformation, and morphologies at the interfaces. Nonlinear simulations under spatially varying electric fields uncover several intriguing self-organized periodic microstructures such as composite core–shell columns, pin-cushion-like structures, membranes with ordered pores, and arrays of open/closed embedded/encapsulated microchannels and microdroplets. Examples of miniaturization of patterns employing patterned electrodes with periodicity less than the spinodal length scales are also shown.



I. INTRODUCTION

The instabilities induced by van der Waals force^{1–59} and externally applied electric field^{60–101} in thin films have emerged as potential techniques to engineer periodic micro/nano structures. These patterns find diverse applications in variety of areas including optoelectronic devices, drug delivery, microfluidics, and patterned functional surfaces, among others.

Previous studies show that an ultrathin (<100 nm) single layer of polymer film can self-organize into randomly placed droplets under the influence of van der Waals force.^{1–10} In comparison, the dewetting of ultrathin bilayers leads to embedded and encapsulated micro/nano architectures.^{11–34} The computational^{35–45} and experimental^{46–59} studies have shown that physico-chemical patterns on the substrate can direct self-organized ordered structures by dewetting. A number of recent studies^{60–101} reveal that electric field lithography (EFL) is another alternative where an externally applied electric field can generate columnar structures with a hexagonal ordering at the free surface of a polymer film. Various other types of patterns including pattern miniaturization are observed in single thin films when the applied field is spatially varying.^{70,71,77,79–81,86,87} Importantly, EFL has an advantage over the other self-organization-based methods because not only can it destabilize ultrathin to relatively thick films (micrometer-size) but also the destabilizing force field and thus the pattern morphology can be controlled by tuning the applied voltage bias.

A few recent studies^{87–89,93–101} have shown that interesting embedded and encapsulated structures can be generated from the electric field induced instabilities of the multilayer thin films. For example, when a bilayer is subjected to an electric field, complex core–shell,^{78,85,86,93–101} hierarchical,^{87,94,96,100} cage-like,⁸⁹ and phase inverted columnar^{88,96} structures are formed. A theoretical study³¹ on three stratified ultrathin liquid films confined between two parallel plates has shown breakup of the interior film into droplets under the influence of intermolecular forces. A recent experimental study¹⁰¹ has explored the electrohydrodynamic instabilities in sequential destabilization of the trilayer assembly (polymer/polymer/polymer/air) in a layer-by-layer approach and reported fabrication of well controlled, self-organized, hierarchical nanostructures.

The instabilities of the confined trilayer under an external electric field have not been explored thus far either experimentally or theoretically. Figure 1 shows the schematic diagram of the three thin viscous films with two deformable liquid–liquid interfaces between the patterned electrodes. The trilayer can be viewed as the confined bilayer^{85–89,93,94,96,97,100} or two interacting layers^{95,100} where the air gap either on top of the bilayer (film 3 in Figure 1) or in the middle (film 2 in Figure 1) of

Received: June 13, 2012

Revised: September 22, 2012

Published: October 2, 2012

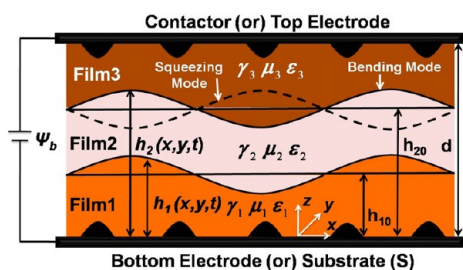


Figure 1. Schematic diagram of a bilayer under the influence of a static electric field applied through patterned top and bottom electrodes. The mean, local thicknesses of the lower and upper liquid/liquid interfaces with flat [Patterned] electrodes are h_{10} , $h_1(x,y,t)$ [$h_{10}-a_1f_1(x,y)$, $h_1(x,y,t)-a_1f_1(x,y)$], and h_{20} , $h_2(x,y,t)$, respectively. d [$d-(a_2f_2+a_1f_1)$] is the distance between flat [patterned] electrodes. The in-phase solid line and the antiphase dotted line at the upper liquid/liquid interface indicate *bending* and *squeezing* mode of evolution with respect to the lower interface. The solid horizontal lines at both of the interfaces indicate the base state.

interacting layers is filled by a third liquid. As will be shown, the additional liquid layer adds flexibility in controlling dielectric contrast across the interfaces, reduces the stabilizing influence of surface tensions thus helping in miniaturization of the microstructures, and allows fabrication of a wider variety of morphologies.

In the present study, a generalized linear stability analysis (LSA) is carried out for the trilayer, which uncovers the sensitivity of the length and time scales of instabilities with the viscosities, surface tensions, dielectric permittivities, and thicknesses of the layers. Following this, a nonlinear analysis based on lubrication approximation is presented where a set of coupled nonlinear equations are derived that describe the evolution of the two deformable interfaces. A long-wave dispersion relation is also obtained by linearizing the evolution equations and compared with the results of the generalized LSA. Furthermore, 2-D and 3-D nonlinear simulations are performed to study the evolution of interfaces into micro/nano structures. The ordering of these structures is also studied by imposing topographically patterned electrodes. The study uncovers the conditions to fabricate many interesting and complex mesostructures by preferential removal of the constitutive layers.

II. PROBLEM FORMULATION

In this section, the governing equations and the boundary conditions are formulated for the trilayer system (Figure 1) subjected to a destabilizing homogeneous or heterogeneous (laterally varying) electric field. The liquid films are considered to be perfectly dielectric, isothermal, and incompressible Newtonian liquids. The Newtonian liquid behavior is assumed because most of the experiments related to thin film instabilities are performed well above the glass-transition temperature of the polymer used. Owing to the small thicknesses of the films gravity is neglected over the electric field force. However, for the ease of discussion, the films 1 to 3 in Figure 1 are termed as lower, middle, and upper layers, respectively. The films are also assumed to be completely wettable on the substrates. In the formulation, the notations x and y represent the span-wise and transverse coordinates parallel to the substrate, respectively, and z represents the coordinate normal to the substrate. In the equations shown below, the subscript i denotes the respective layer ($i = 1, 2, 3$, and s denotes lower layer, middle layer, upper layer, and solid substrate, respectively). For the layer i , u_i , v_i , and w_i

are the x , y and z components of velocity; μ_i , ρ_i , γ_i , and ϵ_i represent the viscosity, density, surface tension, and dielectric permittivity, respectively. The parameter $P_i = p_i - \pi_i$ is the effective, nonbody force pressure inside the films, p_i denotes the isotropic static pressure in the liquid, and π_i is the pressure from the applied electric field. The subscripts t , x , y , and z in the equations denote differentiation with respect to time and the respective coordinate. The variable thicknesses of the upper interface and lower interface are denoted by h_2 and h_1 , respectively. Thus, $h_M = (h_2 - h_1)$ is the thickness of the middle layer and $h_U = (d - h_2)$ is the thickness of the upper layer. The symbols h_{20} , h_{10} , h_{M0} , and h_{U0} represent the respective constant base state thicknesses. The patterned electrodes are described by the functional form $a_i f_i(x,y)$, as shown in Figure 1, where a_i is the amplitude and $f_i(x,y)$ is a periodic function of wavelength λ_p .

Governing Equations and Boundary Conditions. In the absence of the inertial and gravity terms for thin films ($<10 \mu\text{m}$), the following dimensional momentum and continuity equations in the Stokes flow regime are assumed for each liquid layer

$$-\nabla P_i + \nabla \cdot \bar{\tau}_i = 0 \text{ and } \nabla \cdot \mathbf{u}_i = 0 \quad (1)$$

where for the i th layer, $\bar{\tau}_i = \mu_i (\nabla \mathbf{u}_i + \nabla \mathbf{u}_i^T)$ is the stress tensor and $\mathbf{u}_i \{u_i, v_i, w_i\}$ is the velocity vector. No-slip and impermeability boundary conditions ($\mathbf{u}_1 = 0$) and ($\mathbf{u}_3 = 0$) are applied at $z = a_1 f_1$ (bottom electrode) and $z = (d - a_2 f_2)$ (top electrode), respectively. Continuity of velocities ($\mathbf{u}_1 = \mathbf{u}_2$), shear stress balance ($\mathbf{t}_1 \cdot \bar{\tau}_2 \cdot \mathbf{n}_1 = \mathbf{t}_1 \cdot \bar{\tau}_1 \cdot \mathbf{n}_1$), normal stress balance ($\mathbf{n}_1 \cdot \bar{\tau}_2 \cdot \mathbf{n}_1 - \mathbf{n}_1 \cdot \bar{\tau}_1 \cdot \mathbf{n}_1 = \gamma_{21} \kappa_1$), and the kinematic condition ($\dot{h}_1 + u_1 (\partial h_1 / \partial x) = w_1$) are enforced at $z = h_1$ (lower interface). Finally, continuity of velocities ($\mathbf{u}_2 = \mathbf{u}_3$), the shear stress balance ($\mathbf{t}_2 \cdot \bar{\tau}_3 \cdot \mathbf{n}_2 = \mathbf{t}_2 \cdot \bar{\tau}_2 \cdot \mathbf{n}_2$), the normal stress balance ($\mathbf{n}_2 \cdot \bar{\tau}_3 \cdot \mathbf{n}_2 - \mathbf{n}_2 \cdot \bar{\tau}_2 \cdot \mathbf{n}_2 = \gamma_{32} \kappa_2$), and the kinematic condition ($\dot{h}_2 + u_2 (\partial h_2 / \partial x) = w_2$) are enforced at $z = h_2$ (upper interface). Here κ_i is curvature, $\mathbf{n}_i [(-h_{ix}, 1) / (1 + h_{ix}^2)^{1/2}]$ and $\mathbf{t}_i [(1, h_{ix}) / (1 + h_{ix}^2)^{1/2}]$ are normal and tangent vectors, and the symbol ∇ is the gradient operator. The superscript dot in the expressions represents the time derivative of the variables. γ_{ij} is the interfacial tension at the liquid–liquid interface.

Excess Pressures Engendered By the Electric Field.

Assuming that the time scale for magnetic field is much smaller than that for the electrical phenomena and electroneutrality in the bulk prevails for all fluids, the following governing equations are appropriate for the electric field, E^{90}

$$\nabla \cdot \mathbf{E}_i = 0, \quad i = 1, 2, \text{ and } 3 \quad (2)$$

Because the electric fields are irrotational ($\nabla \times \mathbf{E}_i = 0$), they can be written in terms of a potential functions ψ_i as $\mathbf{E}_i = -\nabla \psi_i$, which leads to the following Laplace equations for the potentials ψ_i from eq 2

$$\nabla^2 \psi_i = 0 \quad (3)$$

This Laplace equation is solved by using the boundary conditions: $\psi_1 = \psi_b$ and $\psi_3 = 0$ at $z = a_1 f_1$ and $z = (d - a_2 f_2)$, respectively, and continuity of tangential and the normal components of the electric field at the lower and upper interfaces, that is, $\psi_1 = \psi_2$ and $\epsilon_1 (\partial \psi_1 / \partial z) = \epsilon_2 (\partial \psi_2 / \partial z)$ at $z = h_1$ and $\psi_2 = \psi_3$ and $\epsilon_2 (\partial \psi_2 / \partial z) = \epsilon_3 (\partial \psi_3 / \partial z)$ at $z = h_2$. Here ϵ_i are the dielectric constant of the fluids $i = 1, 2$, and 3 and ψ_b is the voltage applied across the two electrodes. The expressions for the electrical potentials obtained after solving eq 3 are

$$\begin{aligned}
\psi_1 &= \psi_b [(-\varepsilon_2 \varepsilon_3 z / (h_2 \varepsilon_1 [\varepsilon_3 - \varepsilon_2] + (h_1 - a_{1f_1}) \varepsilon_3 [\varepsilon_2 - \varepsilon_1] \\
&\quad + \varepsilon_2 \varepsilon_1 (d - a_{2f_2}))) + 1] \\
\psi_2 &= -\psi_b [(\varepsilon_1 \varepsilon_3 z + \varepsilon_1 ((\varepsilon_2 - \varepsilon_3) h_2 - \varepsilon_2 d)) \\
&\quad / (h_2 \varepsilon_1 [\varepsilon_3 - \varepsilon_2] + (h_1 - a_{1f_1}) \varepsilon_3 [\varepsilon_2 - \varepsilon_1] \\
&\quad + \varepsilon_2 \varepsilon_1 (d - a_{2f_2}))] \\
\psi_3 &= -\psi_b [\varepsilon_1 \varepsilon_2 (z - d) / (h_2 \varepsilon_1 [\varepsilon_3 - \varepsilon_2] \\
&\quad + (h_1 - a_{1f_1}) \varepsilon_3 [\varepsilon_2 - \varepsilon_1] + \varepsilon_2 \varepsilon_1 (d - a_{2f_2}))]
\end{aligned} \quad (4)$$

The expressions for the potentials in eq 4 are further utilized to obtain the excess pressures at the two deformable interfaces for the spatially varying electric field

$$\begin{aligned}
\pi_1 &= -\frac{\varepsilon_0}{2} \left[\varepsilon_1 \left(\frac{\partial \psi_1}{\partial z} \right)^2 - \varepsilon_2 \left(\frac{\partial \psi_2}{\partial z} \right)^2 \right] \\
&= - \left[\frac{\varepsilon_0 \varepsilon_1 \varepsilon_2 \varepsilon_3^2 \psi_b^2 [\varepsilon_2 - \varepsilon_1]}{2 [h_2 \varepsilon_1 [\varepsilon_3 - \varepsilon_2] + (h_1 - a_{1f_1}) \varepsilon_3 [\varepsilon_2 - \varepsilon_1] + \varepsilon_2 \varepsilon_1 (d - a_{2f_2})]^2} \right]
\end{aligned} \quad (5)$$

$$\begin{aligned}
\pi_2 &= -\frac{\varepsilon_0}{2} \left[\varepsilon_2 \left(\frac{\partial \psi_2}{\partial z} \right)^2 - \varepsilon_3 \left(\frac{\partial \psi_3}{\partial z} \right)^2 \right] \\
&= - \left[\frac{\varepsilon_0 \varepsilon_1^2 \varepsilon_2 \varepsilon_3 \psi_b^2 [\varepsilon_3 - \varepsilon_2]}{2 [h_2 \varepsilon_1 [\varepsilon_3 - \varepsilon_2] + (h_1 - a_{1f_1}) \varepsilon_3 [\varepsilon_2 - \varepsilon_1] + \varepsilon_2 \varepsilon_1 (d - a_{2f_2})]^2} \right]
\end{aligned} \quad (6)$$

Here ε_0 is the permittivity of free space. The electric field for homogeneous electrodes is obtained by setting $a_{if_i}(x, y) = 0$.

Linear Stability Analysis. To get the dispersion relation, the governing equations are linearized using normal linear modes,

$\mathbf{u}_i = \tilde{\mathbf{u}}_i e^{i\omega t + i k x}$, $P_i = \tilde{P}_i e^{i\omega t + i k x}$, and $h_i = h_{i0} + \delta_i e^{i\omega t + i k x}$ where the symbols ω and k represent the linear growth rate coefficient and the wavenumber of disturbance, respectively. Furthermore, it is assumed that the kinematics of deformation of the films is treated using a small-deformation formulation and the excess pressures are expanded in Taylor series about the base state and terms up to first order are retained.^{94,95}

$$\begin{aligned}
\pi_j(h_{10} + \delta_1, h_{20} + \delta_2) \\
= \pi_j(h_{10}, h_{20}) + [(\partial \pi_j / \partial h_1)_{h_{10}, h_{20}} \delta_1 + (\partial \pi_j / \partial h_2)_{h_{10}, h_{20}} \delta_2 + \dots]
\end{aligned} \quad (7)$$

where $j = 1$ and 2 and δ_1 and δ_2 are the infinitesimal perturbations at the lower and upper interface, respectively. Eliminating \tilde{P}_i from the linearized governing equations results in a biharmonic equation for each of the three layers ($i = 1, 2$, and 3)

$$\frac{d^4 \tilde{w}_i}{dz^4} - 2k^2 \frac{d^2 \tilde{w}_i}{dz^2} + k^4 \tilde{w}_i = 0 \quad (8)$$

The general solution for eq 8 is

$$\tilde{w}_i = (B_{i1} + B_{i2} z) e^{kz} + (B_{i3} + B_{i4} z) e^{-kz} \quad (9)$$

where the coefficients B_{ij} ($i = 1, 2$, and 3 ; $j = 1$ to 4) are constants. Replacing the expressions for \tilde{w}_i , \tilde{u}_i , and \tilde{P}_i in the linearized boundary conditions leads to a set of 12 homogeneous linear algebraic equations involving 12 unknown constants. Equating the determinant of this matrix to zero, the dispersion relation for the trilayer is obtained, as shown by eq 10. The details of the derivation done by employing the commercial package Mathematica are provided in Part A of the Supporting Information.

$$\begin{bmatrix}
-\frac{e^{-J} G_1}{2k} & \frac{G_2}{2k} & -e^{-J} & -h_1 e^{-J} & -e^{-J} & -h_1 e^{-J} & 0 & 0 \\
-\frac{e^{-J} G_3}{2k} & \frac{G_4}{2k} & e^{-J} & \frac{e^{-J}(-1+J)}{k} & -e^J & \frac{e^J(1+J)}{k} & 0 & 0 \\
0 & 0 & e^{-Q} & h_2 e^{-Q} & e^Q & h_2 e^Q & \frac{G_5}{2k} & \frac{G_6}{2k} \\
0 & 0 & -e^{-Q} & -\frac{e^{-Q}(-1+Q)}{k} & e^Q & \frac{e^Q(1+Q)}{k} & \frac{G_7}{2k} & \frac{G_8}{2k} \\
-e^{-J} G_9 & G_{10} & -2e^{-J} k & -2e^{-J}(-1+J) & -2ke^J & -2e^J(1+J) & 0 & 0 \\
0 & 0 & 2e^{-Q} k & 2e^{-Q}(1+Q) & 2e^Q k & 2e^Q(1+Q) & G_{11} & G_{12} \\
\frac{G_{13}}{2k\omega} & \frac{G_{14}}{2k\omega} & -2e^{-J} k + \frac{e^{-Q} \phi_2}{\omega} & -2e^{-J} J + \frac{e^{-Q} h_2 \phi_2}{\omega} & 2e^J k + \frac{e^Q \phi_2}{\omega} & 2e^J J + \frac{e^Q h_2 \phi_2}{\omega} & 0 & 0 \\
\frac{G_{15}}{2k\omega} & \frac{G_{16}}{2k\omega} & \frac{e^{-Q}(2k\omega + \phi_4)}{\omega} & \frac{e^{-Q} h_2(2k\omega + \phi_4)}{\omega} & \frac{e^Q(-2k\omega + \phi_4)}{\omega} & \frac{e^Q h_2(2k\omega - \phi_4)}{\omega} & G_{17} & G_{18}
\end{bmatrix} = 0 \quad (10)$$

III. NONLINEAR LONG-WAVE ANALYSIS

In this section, the coupled evolution equations for the lower and upper liquid–liquid interfaces subjected to heterogeneous electric field are derived by extending the standard procedure

employed for the long-wave analysis in thin films.^{6–8,35–43} The assumptions made for this derivation are (i) the layers are thin enough that convective terms can be neglected and (ii) the long-wave approximation is valid because all interfacial deformations have small slope. The long-wave momentum, $\mu_i \mu_{izz} = (p_i + \phi_i)_x$

and $\mu_i u_{izz} = (p_i + \phi_i)_y$, continuity, $\nabla \cdot \mathbf{u}_i = 0$, and the kinematic conditions at the two interfaces, $\dot{h}_i = -u_i(\partial h_i / \partial x) + w_i$ lead to the evolution equations for interfaces, $h_j = h_j(x, y, t)$, where $i = 1, 2$, and 3 and $j = 1$ and 2. The long-wave boundary conditions employed for this derivation are: $\mathbf{u}_1 = 0$ and $\mathbf{u}_3 = 0$ at $z = q = a_1 f_1$ and $z = g = (d - a_2 f_2)$, respectively (no-slip and impermeability at the patterned top and bottom electrodes); $\mathbf{u}_1 = \mathbf{u}_2$, $\mu_2 u_{2z} = \mu_1 u_{1z}$, and $\mu_2 v_{2z} = \mu_1 v_{1z}$ all at $z = h_1$ (continuity of velocity and shear stress at lower interface); and $\mathbf{u}_2 = \mathbf{u}_3$, $\mu_3 u_{3z} = \mu_2 u_{2z}$, and $\mu_3 v_{3z} = \mu_2 v_{2z}$ at $z = h_2$ (continuity of velocity and shear stress at upper interface). The evolution equations that describe the stability, dynamics, and morphology of the coupled deformable interfaces of a trilayer are

$$\begin{aligned} \frac{\partial h_1}{\partial t} + \nabla \left[\frac{\nabla P_1}{2r} \left(\frac{(q - h_1)^3}{6} \left[(h_1 - q) \frac{\mu_2 \mu_3}{\mu_1} + 4(g - h_2) \mu_2 + 4(h_2 - h_1) \mu_3 \right] \right) \right. \\ \left. + \frac{\nabla P_2}{2r} \left(\frac{(q - h_1)^2}{2} (h_2 - h_1) [2(h_2 - g) \mu_2 + (h_1 - h_2) \mu_3] \right) \right. \\ \left. + \frac{\nabla P_3}{2r} \left(-\frac{(q - h_1)^2}{2} [(g - h_2)^2 \mu_2] \right) \right] = 0 \end{aligned} \quad (11)$$

$$\begin{aligned} \frac{\partial h_2}{\partial t} + \nabla \left[\frac{\nabla P_1}{2r} \left(\frac{(g - h_2)^2}{2} [(q - h_1)^2 \mu_2] \right) \right. \\ \left. + \frac{\nabla P_2}{2r} \left(\frac{(g - h_2)^2}{2} (h_1 - h_2) [2(q - h_1) \mu_2 + (h_1 - h_2) \mu_1] \right) \right. \\ \left. + \nabla \left[\frac{\nabla P_3}{2r} \left(\frac{(g - h_2)^3}{6} \left[4(h_1 - q) \mu_2 + (g - h_2) \frac{\mu_1 \mu_2}{\mu_3} \right. \right. \right. \right. \\ \left. \left. \left. + 4(h_2 - h_1) \mu_1 \right] \right) \right] \right] = 0 \end{aligned} \quad (12)$$

where $r = [(h_1 - q) \mu_2 \mu_3 + (g - h_2) \mu_1 \mu_2 + (h_2 - h_1) \mu_1 \mu_3]$. The pressure gradients (P_i) are derived from the normal stress balances at the interfaces along with the equation for total mass conservation to obtain the base state pressure³¹

$$P_1 - P_2 = -\gamma_{21} \nabla^2 h_1 + \left[\frac{\varepsilon_0 \varepsilon_1}{2} \left(\frac{\partial \psi_1}{\partial z} \right)^2 - \frac{\varepsilon_0 \varepsilon_2}{2} \left(\frac{\partial \psi_2}{\partial z} \right)^2 \right] \quad (13)$$

$$P_2 - P_3 = -\gamma_{32} \nabla^2 h_2 + \left[\frac{\varepsilon_0 \varepsilon_2}{2} \left(\frac{\partial \psi_2}{\partial z} \right)^2 - \frac{\varepsilon_0 \varepsilon_3}{2} \left(\frac{\partial \psi_3}{\partial z} \right)^2 \right] \quad (14)$$

$$q_1 + q_2 + q_3 = \int_0^{h_1} u_1^x + \int_{h_1}^{h_2} u_2^x + \int_{h_2}^d u_3^x = 0. \quad (15)$$

Here q_i represents flow rates of each layer that are functions of three pressure gradients $\partial P_i / \partial x$ ($i = 1$ to 3) and are obtained by integrating the velocity profile of each layer with respect to z . The expressions for the flow rates are provided in Part B of the Supporting Information.

The long-time interfacial evolution leads to the well-known contact line singularities when any of the interfaces comes in contact with another interface. To remove these nonphysical contact-line singularities, a short-range repulsive van der Waals potential is incorporated.⁷⁰ This strategy allows the formation of a thin precursor (<5 nm) near the zones of contact and thus allows capturing the long-time evolution of the interfaces.

The electric potential combined with a short-range repulsion gives the total disjoining pressures at the two interfaces

$$\begin{aligned} \pi_1 = \left[\frac{-\varepsilon_0 \varepsilon_1 \varepsilon_2 \varepsilon_3^2 \psi_b^2 [\varepsilon_2 - \varepsilon_1]}{2[h_2 \varepsilon_1 [\varepsilon_3 - \varepsilon_2] + (h_1 - q) \varepsilon_3 [\varepsilon_2 - \varepsilon_1] + \varepsilon_2 \varepsilon_1 g]^2} \right] \\ + \frac{A_1}{6\pi(h_1 - q)^3} + \frac{A_2}{6\pi h_2^3} \end{aligned} \quad (16)$$

$$\begin{aligned} \pi_2 = \left[\frac{-\varepsilon_0 \varepsilon_1^2 \varepsilon_2 \varepsilon_3 \psi_b^2 [\varepsilon_3 - \varepsilon_2]}{2[h_2 \varepsilon_1 [\varepsilon_3 - \varepsilon_2] + (h_1 - q) \varepsilon_3 [\varepsilon_2 - \varepsilon_1] + \varepsilon_2 \varepsilon_1 g]^2} \right] \\ + \frac{A_1}{6\pi(h_1 - q)^3} + \frac{A_2}{6\pi(g - h_2)^3} + \frac{A_3}{6\pi(h_2 - h_1)^3} \end{aligned} \quad (17)$$

The inclusion of the short-range repulsion terms is effective only for ultrathin (<5 nm) film and does not affect the evolution of the relatively thicker films considered here, which is dominated entirely by the force exerted by the electric field. Because the polymers considered are perfect dielectrics, the external electric field polarizes the molecules into induced dipoles, which essentially accumulate near the interface to develop electrical stresses. In such a scenario, the bulk of the fluid layers remains electroneutral (the volume charge density will be zero because of the cancellation of equal magnitude positive and negative charges) and the divergence free Gauss law for electrostatics become applicable. The induced dipole moment at the liquid/liquid interfaces results in the generation of excess pressures at these deformable interfaces.^{70,77,94–96}

Long-Wave Linear Stability Analysis. Linearizing eqs 11 and 12 under homogeneous electric field ($q \rightarrow 0$ and $g \rightarrow d$) by the linear normal modes, $h_i = h_{i0} + \delta e^{i\omega t + ikx}$, results in the following long-wave linear dispersion relation²³

$$\omega = \frac{-(B + C) \pm \sqrt{(B - C)^2 + 4AD}}{2} \quad (18)$$

where

$$A = [A_1 K_1 + B_1 K_1 - C_1 (K_2 + K_3)] (-\gamma_{32} k^4 + \pi_{22} k^2) + [A_1 K_2 - B_1 (K_2 + K_3) - C_1 K_2] (\pi_{21} k^2)$$

$$B = [A_1 K_1 + B_1 K_1 - C_1 (K_2 + K_3)] (-\gamma_{21} k^4 + \pi_{21} k^2) + [A_1 K_2 - B_1 (K_2 + K_3) - C_1 K_2] (-\gamma_{21} k^4 + \pi_{11} k^2)$$

$$C = [D_1 K_1 + E_1 K_1 - F_1 (K_2 + K_3)] (-\gamma_{32} k^4 + \pi_{22} k^2) + [D_1 K_2 - E_1 (K_2 + K_3) - F_1 K_2] (\pi_{21} k^2)$$

$$D = [D_1 K_1 + E_1 K_1 - F_1 (K_2 + K_3)] (-\gamma_{21} k^4 + \pi_{21} k^2) + [D_1 K_2 - E_1 (K_2 + K_3) - F_1 K_2] (-\gamma_{21} k^4 + \pi_{11} k^2) \quad (19)$$

Here the expressions for A_1 – F_1 and K_1 – K_3 are provided in Part B of the Supporting Information and $\pi_{ji} = (\partial \pi_j / \partial h_i)$ terms are evaluated at mean thicknesses h_{10} and h_{20} , where i and $j = 1$ or 2. In the absence of substrate heterogeneity, the dispersion relation gives the range of wave numbers of the disturbance where $\omega > 0$. The fastest growth rate of disturbance, ω_m , and the corresponding wavelength, $\lambda_m = 2\pi/k_m$, are obtained by finding out the global maximum of the growth coefficient.

Nondimensional Equations and Numerical Methods. For a compact representation of numerical results, the evolution

eqs 11 and 12 are nondimensionalized by introducing the following nondimensional variables: $T = (\gamma_{21}K^2/3\mu_1h_{10})t$; $\{X,Y\} = (\{x,y\}/h_{10})K^{1/2}$; $\{H_1,H_2,D,Q,G\} = \{h_1,h_2,d,q,g\}/h_{10}$; $\Gamma_r = \gamma_{32}/\gamma_{21}$; $S_1 = \mu_3/\mu_1$; $S_2 = \mu_3/\mu_2$; $S_3 = \mu_2/\mu_1$; $\{\bar{P}_1,\bar{P}_2\} = \{P_1,P_2\}h_{10}/K\gamma_{21}$; and $K = (\varepsilon_0\psi_b^2/2\gamma_{21}h_{10})$.

The resulting nondimensional evolution equations are:

$$\begin{aligned} \frac{\partial H_1}{\partial T} + \frac{3}{2} \nabla \cdot \left[\frac{\nabla \cdot \bar{P}_1}{R} \left(\frac{(Q - H_1)^3}{6} ((H_1 - Q)S_1 + 4(G - H_2) + 4(H_2 - H_1)S_2) \right) \right] \\ + \frac{3}{2} \nabla \cdot \left[\frac{\nabla \cdot \bar{P}_2}{RS_3} \left(\frac{-(H_1 - Q)^2}{2} (H_2 - H_1)(2(G - H_2)S_3 + (H_2 - H_1)S_1) \right) \right] \\ + \frac{\nabla \cdot \bar{P}_3}{RS_1} \left(\frac{-(H_1 - Q)^2}{2} (G - H_2)^2 S_1 \right) \right] = 0 \end{aligned} \quad (20)$$

$$\begin{aligned} \frac{\partial H_2}{\partial T} + \frac{3}{2} \nabla \cdot \left[\frac{\nabla \cdot \bar{P}_1}{R} \left(\frac{(G - H_2)^2}{2} (H_1 - Q)^2 \right) \right] \\ + \frac{\nabla \cdot \bar{P}_2}{RS_3} \left(\frac{(G - H_2)^2}{2} (H_2 - H_1)(2H_1S_3 + (H_2 - H_1)) \right) \right] \\ + \frac{3}{2} \nabla \cdot \left[\frac{\nabla \cdot \bar{P}_3}{RS_1} \left(\frac{(G - H_2)^3}{6} (4(H_1 - Q)S_1 + (G - H_2) \right. \right. \\ \left. \left. + 4(H_2 - H_1)S_2) \right) \right] = 0 \end{aligned} \quad (21)$$

where $R = [(H_1 - Q)S_1 + (G - H_2) + (H_2 - H_1)S_2]$.

The nondimensional coupled eqs 20 and 21 were solved numerically to obtain the 2-D and 3-D interfacial morphologies. These equations were discretized using a central difference scheme with half node interpolation. Furthermore, time integration of the resulting set of coupled stiff ordinary differential equations is performed using Gear's algorithm. The simulations were initialized with a volume preserving small amplitude random perturbation at the interfaces and periodic boundary conditions were enforced at the lateral boundaries. The numerical accuracy and convergence was ensured by varying the number of grid points and in most of the cases, ~ 200 (30×30) grid points per Λ were found to be satisfactory for 2-D (3-D) simulations.

The general dispersion relation of the LSA as well as the coupled nonlinear equations can be reduced to the simpler cases of single layer,^{70,77} bilayer,^{94,96,97} and interacting layer⁹⁵ results in the respective asymptotic limits. For example, curves 1 and 2 in Figure 2a show that the length scale of a bilayer can be accurately obtained from the dispersion relation of a trilayer in the asymptotic limit where the dielectric permittivity and the viscosity of the upper layer are significantly small.⁹⁴ The curves 1a and 2a show that the presence of the upper layer in a trilayer can reduce the length scale significantly. Figure 2b conveys that with further increase in the field strength (reducing d) the electric-field-induced instabilities of a trilayer can indeed lead to nanoscale structures. The nonlinear simulation in the images (c) and (d) reproduces the final morphologies of a bilayer⁹⁴ with $\varepsilon_1 < \varepsilon_2$ and $\varepsilon_1 > \varepsilon_2$ by using the evolution eqs 20 and 21 in the asymptotic limit when the upper layer of a trilayer has low dielectric permittivity and viscosity. Figure 2 shows that the dispersion relation and the evolution equations of a trilayer can correctly reproduce the results of a bilayer in one of its asymptotic limits and introduction of the third layer can indeed further reduce the wavelength to the nanoscale.

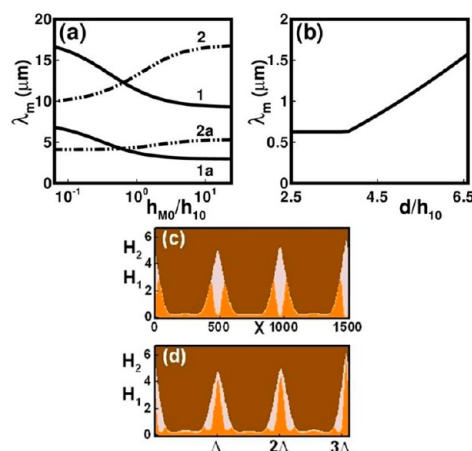


Figure 2. (a) Variation of λ_m with $H_r (= h_{M0}/h_{10})$ at constant h_{20} (500 nm). Curves 1 and 2 correspond to a bilayer asymptotically obtained from the trilayer at the limit $\Gamma_r = 10$ and, curves 1a and 2a correspond to trilayer where $\Gamma_r = 1$. The curves 1 (1a) and 2 (2a) correspond to $\varepsilon_1 = 2.0, \varepsilon_2 = 3.0, \varepsilon_3 = 1.2$ and $\varepsilon_1 = 3.0, \varepsilon_2 = 2.0, \varepsilon_3 = 1.2$, respectively. (b) Variation of λ_m with changing gap between the electrodes when $h_{10} = 150$ nm, $h_{M0} = 100$ nm, $\mu_1 = \mu_2 = \mu_3 = 1$ Pa s, and $\varepsilon_1 = 2.0, \varepsilon_2 = 4.0, \varepsilon_3 = 2.0$. (c,d) 2-D spatiotemporal evolution of instability bilayer asymptotically obtained from the trilayer in a 3Λ domain when $\varepsilon_1 = 2.0, \varepsilon_2 = 3.0, \varepsilon_3 = 1.2$ and $\varepsilon_1 = 3.0, \varepsilon_2 = 2.0, \varepsilon_3 = 1.2$, respectively, when $\Gamma_r = 10$. (a,c,d) $\mu_1 = \mu_2 = 1$ Pa s, $\mu_3 = 0.01$ Pa s, $h_{10} = 150$ nm, $h_{M0} = 100$ nm, and $d = 1$ μm .

IV. RESULTS AND DISCUSSION

The trilayer can be considered to be a capacitor with three plane-parallel layers of dielectric materials constituting the undeformed base state. In the absence of the flow of any charge across the films, the applied electric field can only induce charge separation at the interfaces whereas electroneutrality prevails at the bulk. The interfaces undergo deformation as a measure of stress relaxation and deform more toward the material with lower dielectric permittivity. The following results based on the LSA and nonlinear simulations emphasize that a trilayer can indeed lead to a much wider variety of complex embedded and encapsulated patterns that are otherwise not possible or difficult to materialize by other existing methodologies. Unless otherwise mentioned during the discussion, typical values of the parameters chosen for the linear and nonlinear analysis are $\varepsilon_0 = 8.85 \times 10^{-12}$ C²/N m², $\psi_b = 50$ V, $\gamma_{21} = 0.003$ N/m, $\mu_1 = \mu_2 = \mu_3 = 1$ Pa s, and $h_{10} = h_{M0} = h_{U0} = 1000$ nm.

Linear Stability Analysis. In this section, we explore the effect of viscosities, interfacial tensions, dielectric permittivities, and thicknesses of the individual layers on time and length scale of instabilities in a trilayer. It is important to note here that unlike a single layer or a bilayer the trilayer can be a symmetric system when the physical properties and thicknesses of liquid 1 and 3 are similar and the middle layer is different. The interfaces can also deform in an asymmetric manner when the physical properties or the film thicknesses are different in all layers. The results discussed in the following section are compared, contrasted, and arranged based on the key features of the symmetric and asymmetric trilayers.

Figure 3 shows the LSA results when the thermodynamic parameters such as thicknesses and the dielectric constants of the films are varied. Plots a and d in the Figure 3 show the variation of ω with k , plots b and e show the variation of ω_m with h_{M0}/h_{10} and $\varepsilon_3/\varepsilon_2$, and plots c and f show the variation in λ_m with h_{M0}/h_{10} and $\varepsilon_3/\varepsilon_2$. It is instructive to note that at a fixed d and ψ_b , increasing

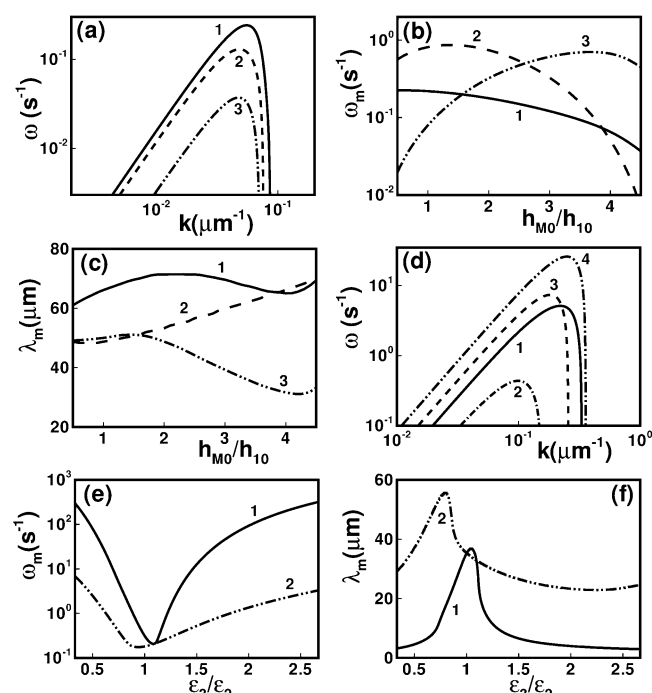


Figure 3. (a,d) Growth rate curves (ω with k). In plot a, Curves 1–3 correspond to $h_{M0} = 0.5, 3$, and $4.5 \mu\text{m}$, respectively, at constant $h_{10} = 1 \mu\text{m}$, $d = 6 \mu\text{m}$, and $\epsilon_1 = 3, \epsilon_2 = 4, \epsilon_3 = 5$. In plot d, Curves 1–4 correspond to $\epsilon_3 = 2, 4, 6$, and 8 , respectively, when $\epsilon_1 = 3, \epsilon_2 = 4$, and $\Gamma_r = 1$. Plot b (c) shows the variation of ω_m [λ_m] with h_{M0}/h_{10} when $\Gamma_r = 1, h_{10} = 1 \mu\text{m}$, and $d = 6 \mu\text{m}$. In plots b and c, curves 1–3 correspond to $\epsilon_1 = 3.0, \epsilon_2 = 4.0, \epsilon_3 = 5.0$; $\epsilon_1 = \epsilon_2 = 3.0, \epsilon_3 = 5.0$ and $\epsilon_1 = \epsilon_3 = 3.0, \epsilon_2 = 5.0$, respectively. Plot e [(f)] shows the variation of ω_m [λ_m] with ϵ_3/ϵ_2 , when $\epsilon_1 = 4.0, \epsilon_2 = 3.0$. In plots e and f curves 1 and 2 correspond to $\Gamma_r = 1$ and 10 , respectively.

the thickness of the film having larger dielectric constant increases the total capacitance (C) of the system. Thus, the strength of the destabilizing electric field increases as the excess free energy ($\Delta G = -0.5C\psi_b^2$) increases. Curve 3 in the plots b and c shows that for a symmetric trilayer, when the thickness of the middle layer with the highest dielectric constant is increased, a larger destabilizing influence progressively increases ω_m and decreases λ_m . In comparison, curves 1 and 2 in Figure 3b,c show that when the thickness of the middle (upper) layer with the lower (higher) dielectric constant is increased (reduced) at a fixed d , ω_m decreases and λ_m increases because of the reduction in the destabilizing electric field strength in an asymmetric trilayer. Curves 1 and 2 in Figure 3c show that λ_m is reduced nearly by two times by merely changing the system from asymmetric to symmetric in terms of the dielectric constants. Plots (d–f) show that changing the dielectric-contrast across the interfaces can also alter the strength of the destabilizing electric field by varying the induced charge separation, which in turn can significantly change the length and time scales. For example, when ϵ_3 is progressively increased to reduce the dielectric-contrast between layers 2 and 3, ω_m (λ_m) initially decreases (increases) to a minimum (maximum) value until the dielectric-contrast becomes zero between the middle and upper films (curves 1 and 2 in the Figure 3d, curve 1 in the Figures 3e,f). However, when ϵ_3 is further increased, the additional electrical stresses again increase the ω_m (reduces λ_m). The value of ϵ_3/ϵ_2 at which the minimum (maximum) of ω_m (λ_m) occurs can be shifted if the ratio of interfacial tensions at the interfaces (Γ_r) is changed, as shown by

the curves 1 and 2 in Figure 3e,f. When the ratio $\epsilon_3/\epsilon_2 = 0.4$, the curves 1 and 2 in Figure 3f contrast the length scales of the confined trilayer and bilayer⁹⁴ systems, respectively. The curves noticeably show a 15 to 20 time reduction in the length scales of the trilayer system compared with that of a bilayer, which is of considerable interest in miniaturization of patterns. The nonlinear simulations discussed later also confirm the time and the length scales commensurate with these LSA predictions. Figure 3 clearly shows that by varying the thermodynamic parameters such as the ratios of the thicknesses, dielectric constants, and the interfacial tensions of the films/interfaces, a wide variety of length scales can be achieved for a trilayer. Most importantly, these length scales are much smaller than the similar bilayer⁹⁴ or interacting layers⁹⁵ because the stabilizing interfacial tensions at the interfaces are at least one order of magnitude lower in the trilayers. Therefore, the structures formed are much finer as compared with the single layer, bilayer, or interacting layer systems of similar materials.

Figure 4 shows the importance of the kinetic parameters such as the viscosity of the films on the length and the time scales of

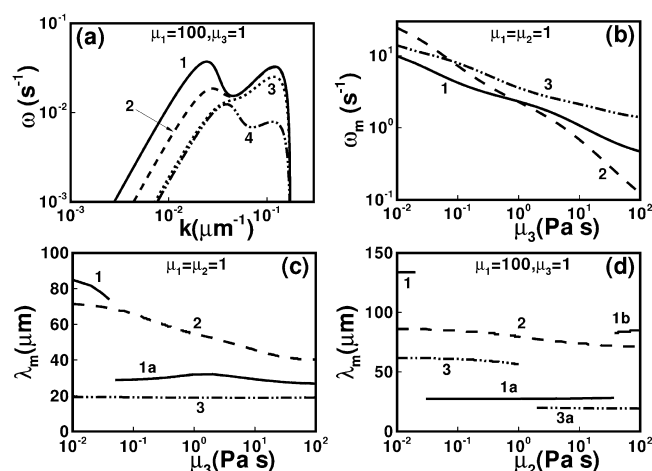


Figure 4. Effect of viscosities on ω_m and λ_m . Plot a shows the growth rate curves (ω with k), where curves 1–4 correspond to $\mu_2 = 0.01, 0.2, 10$, and 100 Pa s , respectively, when $\Gamma_r = 10, \epsilon_1 = 3.0, \epsilon_2 = 4.0$, and $\epsilon_3 = 5.0$. Plot b shows the variation of ω_m with μ_3 when $\Gamma_r = 1$. Plot c [(d)] shows the variation of λ_m with μ_2 [μ_3] when $\Gamma_r = 10$. In plots b–d, the curves 1–3 correspond to $\epsilon_1 = 3.0, \epsilon_2 = 4.0, \epsilon_3 = 5.0$; $\epsilon_1 = 5.0, \epsilon_2 = 4.0, \epsilon_3 = 3.0$; and $\epsilon_1 = \epsilon_3 = 3.0, \epsilon_2 = 5.0$, respectively.

the instability. The ω versus k plots in Figure 4a show that the asymmetric trilayers with dissimilar interfacial tensions ($\Gamma_r = 10$) and viscosities can lead to an interesting bimodal (presence of two maxima) behavior of instability mode selection. As shown later in the simulations, in such situations, the unstable interfaces evolve in a decoupled manner because the interface with higher (lower) interfacial tension picks up the length scale corresponding to the lower (higher) wavenumber. Curve 1 shows the case when the middle layer viscosity, μ , is very small (e.g., 0.01 Pa s) compared with a high μ_1 (100 Pa s) and a moderately high μ_3 (1 Pa s) viscosity of other layers. Although the instability modes are equally dominant in this bimodal case, a smaller (larger) viscous resistance with a larger (smaller) stabilization due to surface tension ensures a larger (smaller) wavenumber instability mode at the upper (lower) interface. Curves 2 and 3 show that increase in μ_2 stabilizes the smaller wavenumber mode much faster than the larger wavenumber mode. In consequence, the dominant mode of instability shifts to the lower interface with

smaller interfacial tension. Furthermore, curve 4 shows that when μ_2 is very high a relatively greater kinetic stabilization of the lower interface shifts the dominant mode of instability to the upper interface where the instability is expected to grow with a smaller wavenumber. Figure 4b–d more clearly shows the shifts when ω_m and λ_m are plotted against the viscosities of the films. Figure 4b shows that with progressive increase in viscosity the ω_m progressively reduces for the trilayers because of increasing viscous resistance. The discontinuities in Figure 4c,d are associated with the jumps from the higher to the lower wavelengths (smaller to larger wavenumbers in a bimodal ω) with the change in μ_2 and μ_3 , respectively. The curves here suggest that when the destabilizing and stabilizing force distribution is dissimilar across the interfaces, changing the viscosity ratio across any of the interface plays a key role in redistribution of the forces. This can either retard or facilitate the growth of the instabilities at the interfaces and in the process influence the length and time scales of instabilities. As a tight summary, the length scale of the instability can be switched from the higher to lower wavelength simply by increasing (decreasing) the viscous resistance significantly across the interface with the higher (lower) interfacial tension, which is encouraging from the applications point of view.

The electric-field-induced instability modes in the trilayers can be: (1) in-phase bending of the interfaces, (2) antiphase squeezing mode, and (3) a mixture of both the bending and squeezing modes that will be called as a mixed mode. LSA predicts these modes correctly, especially in the initial stages of growth when the interfacial deformations are very small, as shown by the previous studies.^{23,26} These modes of deformations and the resulting relative amplitudes of deformations at the interfaces can be correlated to the sign and the magnitude of the ratio of the linear amplitudes of deformations, $\delta_r = \delta_2/\delta_1 = -(\omega + B)/A = -D/(\omega + C)$, where A , B , C , and D are calculated from eq 19 and δ_r is evaluated at ω_m and k_m . The trilayers with $\delta_r > 0$ and $\delta_r < 0$ are expected to evolve in the *bending* and *squeezing* modes of deformations at the onset of instability. In addition, if $|\delta_r| > 1$ ($|\delta_r| < 1$), then the upper (lower) interface deforms more compared with lower (upper) interface.

Figure 5 shows the variations of δ_r with h_{M0}/h_{10} , ϵ_3/ϵ_2 , and μ_2 . Curves 1–3 in Figure 5a predict (i) bending mode ($\delta_r < 0$) of instability when the trilayer is asymmetric and the dielectric permittivity of the middle layer is in-between the lower and the upper layer or same as that of the lower layer and (ii) squeezing mode ($\delta_r > 0$) of instability when the middle layer has the lowest or highest dielectric permittivity among the films. A larger deformation at the upper interface ($|\delta_r| > 1$) is predicted when the destabilizing electric field is relatively higher at the upper interface. Figure 5b shows that when the films are symmetric with respect to thicknesses and viscosities the interfaces evolve in the squeezing mode (curve 1b at $\epsilon_3/\epsilon_2 = 0.55$ and curve 2 at $\epsilon_3/\epsilon_2 = 1.33$). To release the excess electrical stresses generated because of the applied electric field, the film with the highest dielectric constant evolves into the films having lower dielectric constants. Therefore, for symmetric trilayers when the dielectric constant of the middle layer is the lowest, the lower and upper layer fluids evolve toward each other by displacing the middle layer fluid. In contrast, when the dielectric constant of the middle layer is highest, the middle layer evolves toward the electrodes by displacing the lower and upper layer fluids. The squeezing mode prevails with a larger deformation at the interface with the larger dielectric-contrast. Furthermore, the asymmetric trilayers with middle layer having an intermediate dielectric constant always

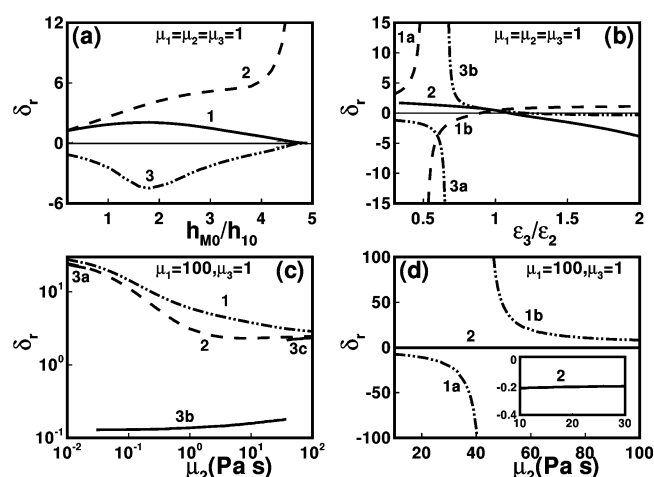


Figure 5. Plot a shows the variation of δ_r with h_{M0}/h_{10} when $\epsilon_1 = 3.0$, $\epsilon_2 = 4.0$, $\epsilon_3 = 5.0$ (curve 1), $\epsilon_1 = \epsilon_2 = 3.0$, $\epsilon_3 = 5.0$ (curve 2) and $\epsilon_1 = \epsilon_3 = 3.0$, $\epsilon_2 = 5.0$ (curve 3) at constant $h_{10} = 1 \mu\text{m}$ and $d = 6 \mu\text{m}$. Plot b shows the variation of δ_r with ϵ_3/ϵ_2 when $\epsilon_1 = 3.0$, $\epsilon_2 = 4.0$ (curve 1), $\epsilon_1 = 4.0$, $\epsilon_2 = 3.0$ (curve 2), and $\epsilon_1 = 3.0$, $\epsilon_3 = 4.0$ (curve 3). In plots a and b, $\Gamma_r = 1$. Plot c [(d)] shows the variation of δ_r with μ_2 when $\epsilon_1 = 3.0$, $\epsilon_2 = 4.0$, $\epsilon_3 = 5.0$ [$\epsilon_1 = \epsilon_3 = 3.0$, $\epsilon_2 = 5.0$]. In plot c, curves 1–3 correspond to $\Gamma_r = 0.1$, 1, and 10, respectively, and in plot d, curves 1 and 2 correspond to $\Gamma_r = 0.1$ and 10, respectively.

evolve in the bending mode in which both the lower and upper interfaces move toward the bottom or top electrode. Again, the larger deformation occurs at the interface where the dielectric-contrast is higher and the interfacial tension is lower. Figure 5c,d shows that for an asymmetric trilayer changing of viscosities can also cause the changeover of modes. The discontinuities in these plots are associated with the bimodality in the ω versus k plots of Figure 4, which also indicates the presence of a mixed mode of instability at the interfaces for these trilayers. In mixed mode, the two interfaces of the trilayer evolve with two different wavelengths at short times, and this scenario can also continue in the later stages of evolutions, as will be shown by the nonlinear simulations discussed below. Figure 5c,d conveys that the relative interfacial deformations and their amplitude can also be controlled by increasing or decreasing the viscous resistances at the interfaces, which is purely a kinetic parameter along with the change in the interfacial tensions. The competition between the strength of the destabilizing electric forces arising from the dielectric contrast across the layers and the stabilizing capillary and viscous forces at the lower and upper interfaces determines the rate of deformation of respective interfaces and thus the modes of evolution.

Morphological Evolution of Interfaces. Interfacial instabilities in trilayers can lead to different morphologies depending on the combinations of film thicknesses, viscosities, dielectric constants and the interfacial tensions. From LSA, we can summarize that the symmetric trilayers with similar physical properties and thicknesses at the upper and the lower layer, and a different material at the middle layer always evolves in the antiphase squeezing mode when the interfacial tensions are the same at the interfaces. However, the parameter space and the control strategies for the completely symmetric trilayers are much more restricted than for the asymmetric trilayers. Introduction of asymmetry to the trilayers in terms of physical properties alters the modes of evolution and amplitudes of deformations at the interfaces, which indicates the possibility to fabricate a host of different morphologies. These structures can

also be ordered by employing patterned electrodes, as previously shown for the single layers and bilayers.^{70,71,77,79–81,94–96,98} In what follows, we discuss the different interesting morphologies for a trilayer under a spatially homogeneous electric field and subsequently ordering of these structures by laterally varying fields produced by patterned electrodes.

Morphologies in Uniform Fields Produced by Planar Electrodes. In this section, the effects of the dielectric permittivities, viscosities, and interfacial tensions of the films on the interfacial morphologies under the influence of a homogeneous electric field are discussed. Unlike in two interacting layer system,⁹⁵ where the interfaces always deform in antiphase squeezing mode, the interfaces of a trilayer can deform either bending or squeezing or in a mixed mode leading to a greater variety of mesostructures.

Figures 6 and 7 show that the choice of the materials can play a significant role in fabricating the microstructures. A minimal

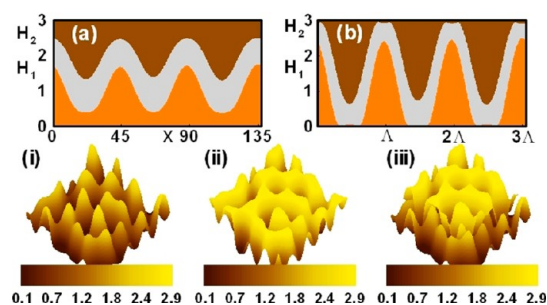


Figure 6. Plots a and b show 2-D spatiotemporal evolution of instability of a trilayer in a 3Λ domain and plots i–iii show 3-D spatiotemporal evolution of instability of lower interface, upper interface, and the composite images, respectively, in a $4\Lambda \times 4\Lambda$ domain when $\epsilon_1 = 3.0$, $\epsilon_2 = 4.0$, and $\epsilon_3 = 5.0$ and $\Gamma_r = 1$. Snapshots of the images given are at times (a) $T = 3.03 \times 10^4$, (b) $T = 1.2 \times 10^5$, and (i–iii) $T = 5.3 \times 10^4$.

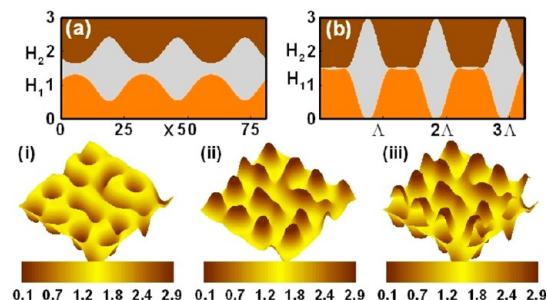


Figure 7. Plots a and b show 2-D spatiotemporal evolution of instability of a trilayer in a 3Λ domain, and plots i–iii show 3-D spatiotemporal evolution of instability of lower interface, upper interface, and the composite images, respectively, in a $4\Lambda \times 4\Lambda$ domain when $\epsilon_1 = 3.0$, $\epsilon_2 = 4.0$, and $\epsilon_3 = 3.0$ and $\Gamma_r = 1$. Snapshots of the images given are at times (a) $T = 4.21 \times 10^4$, (b) $T = 4.98 \times 10^4$, and (i–iii) $T = 2.42 \times 10^6$.

tuning of properties like the dielectric constants of the films can lead to an entirely different structure. Images a and b (images i–iii) in Figure 6 show the evolution of the interfacial instability in a 2-D (3-D) domain having a dimension of 3Λ [$4\Lambda \times 4\Lambda$]. Here Λ is the dimensionless dominant wavelength corresponding to the maximum linear growth coefficient (ω_m). All simulations are initiated with a volume preserving small amplitude random perturbation at the interfaces. In this case, the choice of the dielectric constants ($\epsilon_1 < \epsilon_2 < \epsilon_3$) ensures an asymmetric trilayer. The Figures suggest that in response to the initial

random perturbations, the interfaces select the fastest growing dominant wavelength of evolution when the destabilizing electric field overcomes the stabilizing surface tension forces at the interfaces. The dielectric contrasts across the interfaces ensure that both the interfaces deform by the in-phase bending mode, as previously predicted by the LSA. Because the viscosities of the films are the same for all layers, the kinetics of deformation does not play much role in the mode selection. The 3-D interfacial morphologies in the images i–iii also agree well with the 2-D morphologies and the LSA predictions. The final morphologies shown in images b and iii are particularly difficult to fabricate by interacting layers, and in the case of a confined bilayer, the length scale of such structures is much larger owing to higher stabilizing surface tension force. Furthermore, the equilibrium morphologies in these images show an example of fabricating embedded “serpentine” microchannels exploiting the self-organized instabilities of the trilayer films.

In comparison with Figure 6, Figure 7 shows the evolution of a symmetric trilayer with the middle layer having the largest dielectric constant. Similar to the LSA prediction, the 2-D and 3-D morphologies show that the interfaces evolve in the squeezing mode. The equilibrium morphologies [images (b) and (iii)] show the cavities formed at the lower and the upper layers that are filled with the middle layer liquid. These morphologies are rather difficult to fabricate by a confined bilayer, whereas in an interacting layer setup, the length scale of similar structures is much larger.

Figures 8 and 9 illustrate the effect of viscosities of the layers on the morphological evolution of the interfaces. In the image sets A and B of Figure 8, $\mu_2 = 0.02$ and 50 Pa s, respectively, whereas μ_1 ,

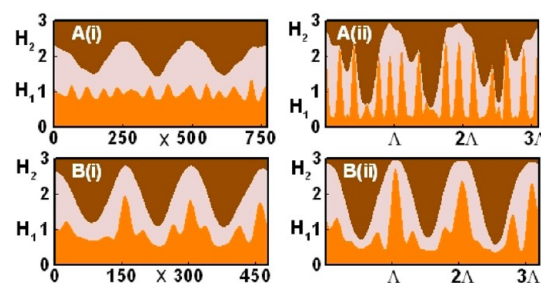


Figure 8. 2-D spatiotemporal evolution of instability of a trilayer in a 3Λ domain when $\epsilon_1 = 3.0$, $\epsilon_2 = 4.0$, and $\epsilon_3 = 5.0$. Plots A and B show the evolution when $\mu_2 = 0.02$ and 50 Pa s, respectively. Snap shots are given at times A(i) $T = 1.43 \times 10^4$, A(ii) $T = 2.87 \times 10^4$, B(i) $T = 5.4 \times 10^4$, and B(ii) $T = 6.62 \times 10^4$. For all plots, $\mu_1 = 100$ Pa s, $\mu_3 = 1$ Pa s, and $\Gamma_r = 10$.

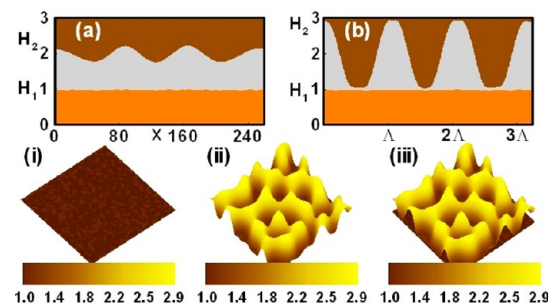


Figure 9. Plots (a) and (b) show 2-D spatiotemporal evolution of instability of a trilayer in a 3Λ domain, and plots i–iii show 3-D spatiotemporal evolution of instability of lower interface, upper interface, and the composite images, respectively, in a $4\Lambda \times 4\Lambda$ domain when $\epsilon_1 = 3.0$, $\epsilon_2 = 4.0$, and $\epsilon_3 = 5.0$. Snapshots of the images given are at times (a) $T = 7.46$, (b) $T = 17.38$, and (i–iii) $T = 5.14 \times 10^5$. The other necessary parameters are $\mu_1 = 10^5$ Pa s, $\mu_2 = \mu_3 = 1$ Pa s, and $\Gamma_r = 1$.

μ_3 , and Γ , were kept constant at 100, 1, and 10 Pa s, respectively. The significant feature noticed in these plots is the evolution of the two interfaces with two different wavelengths, which can be correlated to the bimodality predicted by LSA under similar conditions (Figure 4). The plots show that the lower interface evolves rapidly with a shorter wavelength mode owing to the smaller stabilizing interfacial tension. In contrast, the larger interfacial tension at the upper interface engenders a longer wavelength. Images a and b (i–iii) in Figure 9 show 2-D (3-D) nonlinear simulations for a trilayer with the low-viscosity upper and middle layers ($\mu_2 = \mu_3 = 1$ Pa s) on a very high viscous lower layer ($\mu_1 = 10^5$ Pa s). The images show that even though the dielectric contrasts are the same at both the interfaces $[(\epsilon_3 - \epsilon_2) = (\epsilon_2 - \epsilon_1)]$, the increased viscous resistance at the lower interface reduces the deformation of the lower interface (images a and i). A comparatively faster kinetics helps the upper interface to form columnar structures quickly on the lower layer. The final morphology appears as an array of middle layer columns embedded inside the upper layer liquid and resting on an almost undeformed lower layer (images b and iii). Figures 8 and 9 clearly show that the change in the viscosities, a purely kinetic parameter, can have a profound influence not only on dynamics but also on the morphological and pattern length scale selection.

Morphologies on Topographically Patterned Electrodes. Previous studies^{70,71,77,79–81,94–96,98} have shown that the spatially ordered patterns in single layer, bilayer, and interacting films can be fabricated when topographically patterned electrodes are employed. Because both the electrodes are patterned, the electric-field pressures at the interfaces (eqs 5a and 6a) are functions of the film thicknesses and the spatial coordinates, $\pi_i = f(x, y, h_1, h_M)$. The gradients of the disjoining pressures can thus be written in the following manner^{36,42,44,96}

$$d\pi_i = \left. \frac{\partial \pi_i}{\partial h_1} \right|_{x, y, h_M} dh_1 + \left. \frac{\partial \pi_i}{\partial h_3} \right|_{x, y, h_1} dh_M + \left. \frac{\partial \pi_i}{\partial x} \right|_{y, h_1, h_M} dx + \left. \frac{\partial \pi_i}{\partial y} \right|_{x, h_1, h_M} dy \quad (22)$$

Here $\alpha|_\beta$ implies a variable α evaluated at constant β . The gradients of potentials, ∇P_1 , ∇P_2 , and ∇P_3 , in the eqs 11 and 12 include the forces because of the local film thickness variations (the first two terms in eq 22), which cause a flow from the thinner to thicker regions of the film whenever the spinodal parameter is negative. The forces resulting from the spatial heterogeneity of the electric field (the last two terms in eq 22) lead to the fluid flow from the regions of low to high electric fields. For example, the patterned electrodes impose a higher electrical stress at the zones where the gap between electrodes is small, making the fluids to flow from the regions where the electrode spacing is higher to where it is lower.

Figures 10–12 show the 3-D nonlinear morphological evolution of a trilayer under the influence of the patterned electrodes. The Figures depict the near-to-equilibrium morphologies before the long-time ripening and coalescence takes place among the structures formed. These near-equilibrium structures as well as any intermediate structure can be quenched or cross-linked to make them permanent. Images I–III in Figure 10 show the patterned electrodes with a pattern periodicity (Λ_p), which is chosen to be the same as the spinodal wavelength (μ_3), that is, the dominant dimensionless length scale obtained from the LSA. The image sets (A) and (B) show the spatiotemporal evolution of the asymmetric trilayers, and image sets (C) and (D) show the

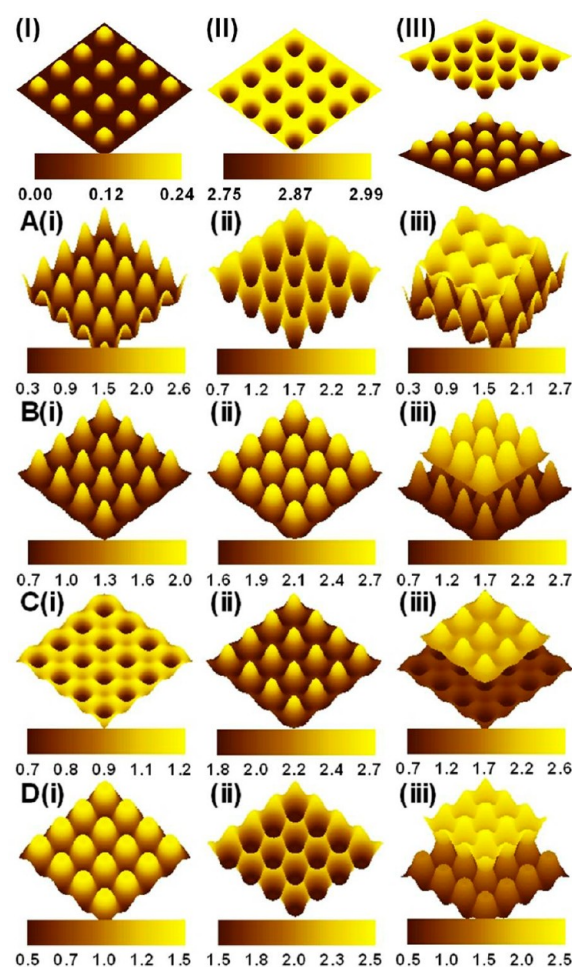


Figure 10. Images I–III show the periodically patterned bottom, top, and composite electrodes, respectively, and the pattern periodicity of the electrodes (Λ_p) is taken to be Λ . Image sets A–D show the surface morphology of a trilayer confined between patterned electrodes in a $4\Lambda \times 4\Lambda$ domain. Plots i–iii in all of the image sets represent the lower interface, upper interface, and the composite images, respectively. For image set A, $\epsilon_1 = 3.0$, $\epsilon_2 = 4.0$, and $\epsilon_3 = 5.0$, for set B, $\epsilon_1 = 5.0$, $\epsilon_2 = 4.0$, and $\epsilon_3 = 3.0$, for set C, $\epsilon_1 = \epsilon_3 = 3$ and $\epsilon_2 = 5.0$, and for set D, $\epsilon_1 = \epsilon_3 = 5$ and $\epsilon_2 = 3.0$. The profiles shown are at (A) $T = 1.61 \times 10^6$, (B) $T = 6.13 \times 10^5$, (C) $T = 2.25 \times 10^5$, and (D) $T = 2.37 \times 10^5$.

same for the symmetric trilayers. The images i–iii in all sets correspond to the morphologies of the lower interface, upper interface, and a composite image of the two interfaces, respectively. The image set (A) shows that the combination of dielectric constants ($\epsilon_1 < \epsilon_2 < \epsilon_3$) ensures that the interfaces are deforming in-phase as both the interfaces deform more toward the bottom electrode. Therefore, the periodic columnar structures formed at the lower interface point to the upper electrode, and the columnar structures at the upper interface point to the bottom electrode. The columns formed at the lower interface are exactly at the interstitial spaces of the columns that are formed at the upper interface. Image set (B) shows that when the films of an asymmetric trilayer have the combination $\epsilon_1 > \epsilon_2 > \epsilon_3$, both the interfaces deform more toward the top electrode and the resulting columns at both the interfaces point to the top electrode. The image sets (A) and (B) convey that either by interchanging the upper and lower layer or simply by changing the direction of the electric field, the direction of the columns at the interfaces can be altered for an asymmetric trilayer. Image set (C) shows that for a

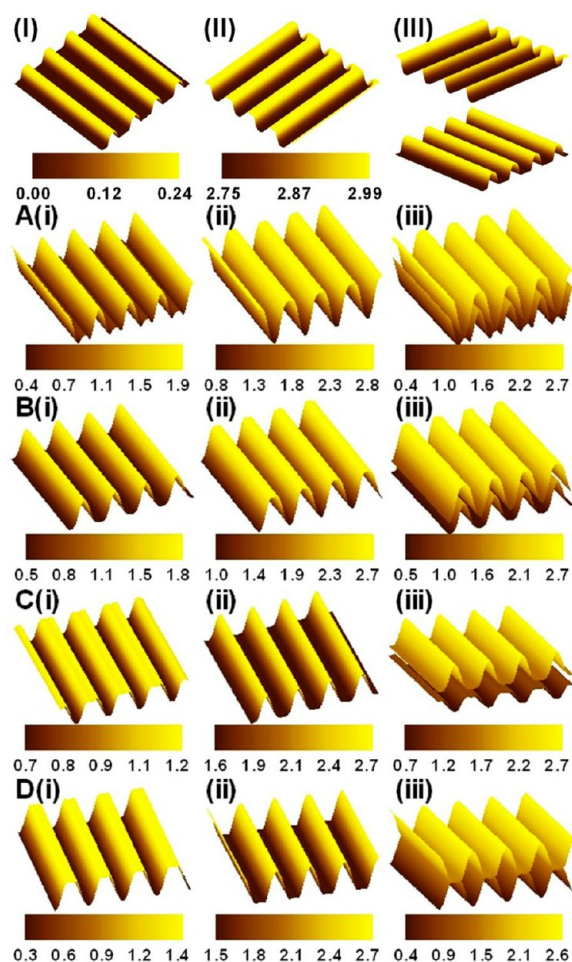


Figure 11. Images I–III show the periodically patterned bottom, top, and composite electrodes, respectively, and the pattern periodicity of the electrodes (Λ_s) is taken to be Λ . Image sets A–D, show the surface morphology of a trilayer confined between striped pattern electrodes in a $4\Lambda \times 4\Lambda$ domain. Plots i–iii in all image sets represent the lower interface, the upper interface, and the composite images, respectively. For image set A, $\epsilon_1 = 3.0$, $\epsilon_2 = 4.0$, and $\epsilon_3 = 5.0$, for set B, $\epsilon_1 = 5.0$, $\epsilon_2 = 4.0$, and $\epsilon_3 = 3.0$, for set C, $\epsilon_1 = \epsilon_3 = 3$ and $\epsilon_2 = 5.0$, and for set D, $\epsilon_1 = \epsilon_3 = 5$ and $\epsilon_2 = 3.0$. The profiles shown are at (A) $T = 2.4 \times 10^6$, (B) $T = 7.67 \times 10^5$, (C) $T = 3.37 \times 10^5$, and (D) $T = 2.54 \times 10^5$.

symmetric trilayer with $\epsilon_1 = \epsilon_3 < \epsilon_2$ the interfaces evolve in the squeezing mode and the lower and the upper layers are penetrated by a periodic array of the middle layer columns growing toward the protruded patterns on the electrodes. In contrast, a symmetric trilayer with the combination, $\epsilon_1 = \epsilon_3 > \epsilon_2$ facilitates penetration of the upper and lower layer columns into the middle layer, as shown by the image set (D). The interfacial morphologies shown in the image sets A–D are interesting because a selective removal of the layers can lead to variety of structures, which includes periodic pin-cushions, encapsulated and embedded droplets, concentric columns, cavities, and so on. The Figures also show that a long-range order can be achieved when the patterned electrodes are employed in contrast with the random patterns generated with homogeneous electrodes (Figures 6 and 7) under similar conditions.

Figure 11 shows the same set of trilayers shown in Figure 10 under electrodes with a striped pattern of periodicity Λ (images I–III). Image sets A and B depict that when $\epsilon_1 < \epsilon_2 < \epsilon_3$ and $\epsilon_1 > \epsilon_2 > \epsilon_3$ the interfaces deform to form an array of in-phase periodic

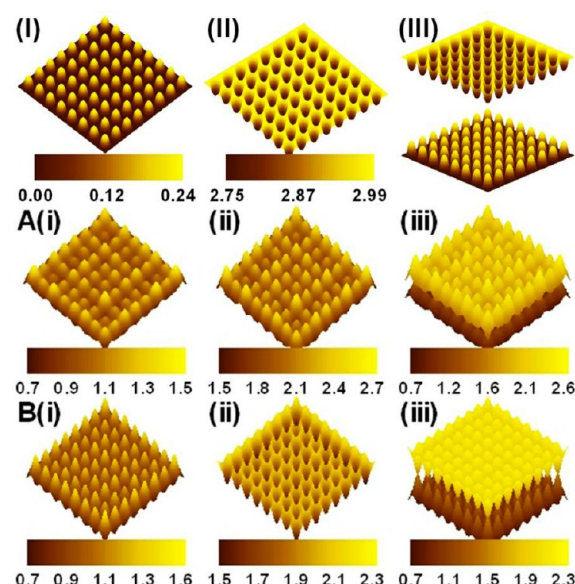


Figure 12. Images I–III show the periodically patterned bottom, top, and composite electrodes, respectively, and the pattern periodicity of the electrodes (Λ_s) is taken to be 0.5Λ . Image sets A and B, show the surface morphology of a trilayer confined between pattern electrodes in a $4\Lambda \times 4\Lambda$ domain. Plots i–iii in both of the image sets represent the lower interface, the upper interface, and the composite images, respectively. For image set A, $\epsilon_1 = 5.0$, $\epsilon_2 = 4.0$, and $\epsilon_3 = 3.0$ and for set B, $\epsilon_1 = \epsilon_3 = 3$ and $\epsilon_2 = 5.0$. The profiles shown are at (A) $T = 1.68 \times 10^6$ and (B) $T = 2.23 \times 10^5$.

longitudinal ridges. It is to be noted that the upper interface is out-of-phase (in-phase) with the top electrode pattern in A (B). The composite structures shown in image sets A and B are interesting because selective removal of the middle or upper or lower layer from the composite structure would result in closed microchannels with a long-range order. Image sets (C) and (D) show that when the dielectric constants of the liquids are changed to $\epsilon_1 = \epsilon_3 < \epsilon_2$ or $\epsilon_1 = \epsilon_3 > \epsilon_2$ the interfaces deform in antiphase squeezing mode and the middle layer forms cylindrical structures. The periodic middle layer cylinders in these cases are also encapsulated by the upper and the lower layer liquids. The morphology shown in image sets (C) and (D) indicates that this type of parametric combination can be employed for preparing self-organized and ordered cylindrical microchannels after selective removal of the middle layer.

Figure 12 shows that when the pattern periodicity on the electrodes is less (0.5Λ) than the spinodal length scale (Λ), there is a possibility of pattern miniaturization of films (images I–III). The image sets A ($\epsilon_1 > \epsilon_2 > \epsilon_3$) and B ($\epsilon_1 = \epsilon_3 < \epsilon_2$) show structures analogous to Figure 10 but now a greater number of structures with much less periodicity as controlled by the electrode-patterns rather than the spinodal length scale. The results in Figure 12 show that the number density of the electric-field-induced patterns can be increased by decreasing the periodicity of the patterns on both of the electrodes. It may be noted that the miniaturization reported here is ~ 15 – 20 times that of the similar interacting layers⁹⁵ or bilayers.^{94,96} However, in the current study, we still employ a trilayer of thicker films ($1 \mu\text{m}$ each) and consider lower field strength (50 V) for comparison. For example, if we consider a trilayer with 50 nm films with the applied voltage of 150 V and with dielectric permittivity and viscosity, as mentioned in the Figure 12, one can fabricate nanostructures with 600 nm periodicity under

homogeneous electrodes and with 300 nm periodicity under patterned electrodes with a periodicity 0.5λ . The pattern periodicity can be reduced further by reducing the thickness of the films or by increasing the field intensity.

V. CONCLUSIONS

A theoretical study is performed on the electric-field-induced instabilities and pattern formation of thin trilayer films. The trilayers are largely classified into two different types, asymmetric and symmetric. Detailed linear and nonlinear analyses have been performed to uncover the effect of thermodynamic parameters such as film thicknesses, viscosities, dielectric constants, and interfacial tensions as well as the kinetic parameters such as viscosities on the time and length scales of the instabilities and the resulting morphologies. The trilayers can reproduce all of the features of the confined bilayers^{85–89,93,94,96,97} or the interacting layers^{95,100} under electric field when the upper layer (film 3 in Figure 1) or the middle layer is replaced by a very low viscosity fluid like air. The additional liquid layer in a trilayer adds more interesting features summarized below:

- (I). Very low contributions from the stabilizing interfacial tensions at the deformable interfaces reduce the length scale (λ_m) of the instability significantly. Therefore, the morphologies are expected to be much more compact as compared with similar confined bilayers^{85–89,93,94,96,97} or the interacting layers.^{95,100} The length scale (λ_m) can also be made shorter by selecting a pair of liquids with a larger dielectric-contrast or by increasing the thickness of the layer with higher dielectric constant. Furthermore, as compared with the confined bilayers or the interacting layers, the third liquid in a trilayer increases the effective capacitance between the electrodes because air is replaced by a material with higher dielectric permittivity. Therefore, the effective destabilizing force is also stronger in the case of a trilayer as compared with similar confined bilayers or the interacting layers, which can cause further miniaturization of the structures.
- (II). The linear and nonlinear analyses together predict some interesting rules for the instability mode selection: (A) When the trilayer is dielectrically asymmetric ($\epsilon_1 > \epsilon_2 > \epsilon_3$ or $\epsilon_1 < \epsilon_2 < \epsilon_3$), the interfaces always evolve by the in-phase bending mode. The interfacial deformations are of similar (different) amplitude when the film thicknesses and viscosities are similar (different). (B) When the trilayer is dielectrically symmetric ($\epsilon_1 > \epsilon_2 < \epsilon_3$ or $\epsilon_1 < \epsilon_2 > \epsilon_3$), the interfaces generally evolve in the antiphase squeezing mode. Again, the interfacial deformations are of similar (different) amplitude when the film thicknesses and viscosities are similar (different). (C) Interfaces evolve in a mixed mode when the interfaces have very different interfacial tensions, and the linear analysis predicts bimodality of the growth rate as a function of the wavenumber. In such a scenario, instabilities at the two interfaces grow with two different wavelengths in which the interface with larger (smaller) interfacial tension picks up the larger (smaller) wavelength. Furthermore, when the instability is of a bimodal nature, the kinetic factors such as viscosity ratio can be tuned to shift the dominant mode of instability from one interface to the other.
- (III). The trilayer configuration offers more control and versatility in generating a variety of open and embedded structures when compared with the electric-field-induced

pattern formation in the confined bilayers or interacting layers. It can of course develop all morphologies that the confined bilayers or interacting layers together can produce as a subset but on much smaller length scales. These intricate self-organized periodic morphologies include arrays of “serpentine”-embedded microchannels, composite core–shell columns, pin-cushion-like structures, membranes with ordered pores, arrays of open/closed embedded microchannels, and embedded microdroplets.

■ ASSOCIATED CONTENT

§ Supporting Information

Steps showing the derivation of dispersion relation through generalized LSA have been provided. Also, the expressions for the flow rates in eq 15 and the expressions for A_1-F_1 and K_1-K_3 in long-wave LSA in Section III are provided. This material is available free of charge via the Internet at <http://pubs.acs.org>.

■ AUTHOR INFORMATION

Corresponding Author

*E-mail: dipban@iitg.ac.in; Phone: +91 361 258 2254 (D.B.).
E-mail: ashutos@iitk.ac.in; Phone: +91 512 259 7026 (A.S.).

Notes

The authors declare no competing financial interest.

■ ACKNOWLEDGMENTS

This work was supported by the DST, New Delhi through its Unit of Excellence on Soft Nanofabrication at IITK and an IRHPA grant. D.B. acknowledges the DST SERC (grant no. SR/S3/CE/0079/2010) for supporting this work.

■ REFERENCES

- (1) Ruckenstein, E.; Jain, R. K. *J. Chem. Soc., Faraday Trans. 2* **1974**, *70*, 132.
- (2) De Gennes, P. G. *Rev. Mod. Phys.* **1985**, *57*, 827.
- (3) Reiter, G. *Phys. Rev. Lett.* **1992**, *68*, 75.
- (4) Brochard-Wyart, F.; Martin, P.; Redon, C. *Langmuir* **1993**, *9*, 3682.
- (5) Sharma, A. *Langmuir* **1993**, *9*, 861.
- (6) Oron, A.; Davis, S. H.; Bankoff, S. G. *Rev. Mod. Phys.* **1997**, *69*, 931.
- (7) Sharma, A.; Khanna, R. *Phys. Rev. Lett.* **1998**, *81*, 3463.
- (8) Thiele, U.; Velarde, M.; Neuffer, K. *Phys. Rev. Lett.* **2001**, *87*, 016104.
- (9) Yang, M. H.; Hou, S. Y.; Chang, Y. L.; Yang, A. C.-M. *Phys. Rev. Lett.* **2006**, *96*, 066105.
- (10) Craster, R. V.; Matar, O. K. *Rev. Mod. Phys.* **2009**, *81*, 1131.
- (11) Higgins, A. M.; Jones, R. A. L. *Nature* **2000**, *404*, 476.
- (12) Lambooy, P.; Phelan, K. C.; Haug, O.; Krausch, G. *Phys. Rev. Lett.* **1996**, *76*, 1110.
- (13) Segalman, R. A.; Green, P. F. *Macromolecules* **1999**, *32*, 801.
- (14) Leopoldes, J.; Damman, P. *Nat. Mater.* **2006**, *5*, 957.
- (15) de Silva, J. P.; Geoghegan, M.; Higgins, A. M.; Krausch, G.; David, M. O.; Reiter, G. *Phys. Rev. Lett.* **2007**, *98*, 267802.
- (16) Xu, L.; Yu, X.; Shi, T. F.; An, L. *Soft Matter* **2009**, *5*, 2109.
- (17) Danov, K. D.; Paunov, V. N.; Alleborn, N.; Raszillier, H.; Durst, F. *Chem. Eng. Sci.* **1998**, *53*, 2809.
- (18) Danov, K. D.; Paunov, V. N.; Stoyanov, S. D.; Alleborn, N.; Raszillier, H.; Durst, F. *Chem. Eng. Sci.* **1998**, *53*, 2823.
- (19) Paunov, V. N.; Danov, K. D.; Alleborn, N.; Raszillier, H.; Durst, F. *Chem. Eng. Sci.* **1998**, *53*, 2839.
- (20) Pototsky, A.; Bestehorn, M.; Merkt, D.; Thiele, U. *Phys. Rev. E* **2004**, *70*, 025201.
- (21) Kumar, S.; Matar, O. K. *J. Colloid Interface Sci.* **2004**, *273*, 581.
- (22) Matar, O. K.; Gkanis, V.; Kumar, S. *J. Colloid Interface Sci.* **2005**, *286*, 319.

- (23) Bandyopadhyay, D.; Gulabani, R.; Sharma, A. *Ind. Eng. Chem. Res.* **2005**, *44*, 1259.
- (24) Pototsky, A.; Bestehorn, M.; Merkt, D.; Thiele, U. *J. Chem. Phys.* **2005**, *122*, 224711.
- (25) Fisher, L. S.; Golovin, A. A. *J. Colloid Interface Sci.* **2005**, *291*, 515.
- (26) Bandyopadhyay, D.; Sharma, A. *J. Chem. Phys.* **2006**, *125*, 054711.
- (27) Pototsky, A.; Bestehorn, M.; Merkt, D.; Thiele, U. *Europhys. Lett.* **2006**, *74*, 665.
- (28) Nepomnyashchy, A. A.; Simanovskii, I. B. *Phys. Fluids* **2006**, *18*, 112101.
- (29) Nepomnyashchy, A. A.; Simanovskii, I. B. *Phys. Fluids* **2006**, *18*, 032105.
- (30) Fisher, L. S.; Golovin, A. A. *J. Colloid Interface Sci.* **2007**, *307*, 203.
- (31) Lenz, R. D.; Kumar, S. *J. Colloid Interface Sci.* **2007**, *316*, 660.
- (32) Bandyopadhyay, D.; Sharma, A. *J. Phys. Chem. B* **2008**, *112*, 11564.
- (33) Nepomnyashchy, A. A.; Simanovskii, I. B. *J. Fluid Mech.* **2009**, *631*, 165.
- (34) Nepomnyashchy, A. A.; Simanovskii, I. B. *Phys. Rev. Lett.* **2009**, *102*, 164501.
- (35) Konnur, R.; Kargupta, K.; Sharma, A. *Phys. Rev. Lett.* **2000**, *84*, 931.
- (36) Kargupta, K.; Sharma, A. *Phys. Rev. Lett.* **2001**, *86*, 4536.
- (37) Kargupta, K.; Sharma, A. *J. Colloid Interface Sci.* **2002**, *245*, 99.
- (38) Kargupta, K.; Sharma, A. *Langmuir* **2002**, *18*, 1893.
- (39) Brusch, L.; Kühne, H.; Thiele, U.; Bär, M. *Phys. Rev. E* **2002**, *66*, 011602.
- (40) Simmons, D.; Chauhan, A. J. *J. Colloid Interface Sci.* **2006**, *295*, 472.
- (41) Saprykin, S.; Trevelyan, P. M. J.; Koopmans, R. J.; Kalliadasis, S. *Phys. Rev. E* **2007**, *75*, 026306.
- (42) Lenz, R. D.; Kumar, S. *J. Fluid Mech.* **2007**, *571*, 33.
- (43) Bandyopadhyay, D.; Sharma, A.; Rastogi, C. *Langmuir* **2008**, *24*, 14048.
- (44) Sarkar, J.; Sharma, A. *Langmuir* **2010**, *26*, 8464.
- (45) Bandyopadhyay, D.; Sharma, A. *J. Phys. Chem. C* **2010**, *114*, 2237.
- (46) Reiter, G.; Auroy, P.; Auvray, L. *Macromolecules* **1996**, *29*, 2150.
- (47) Sehgal, A.; Ferreira, V.; Douglas, J. F.; Amis, E. J.; Karim, A. *Langmuir* **2002**, *18*, 7041.
- (48) Wunnicke, O.; Müller-Buschbaum, P.; Wolkenhauer, M.; Lorenz-Haas, C.; Cubitt, R.; Leiner, V.; Stamm, M. *Langmuir* **2003**, *19*, 8511.
- (49) Kim, D. H.; Kim, M. J.; Park, J. Y.; Lee, H. H. *Adv. Funct. Mater.* **2005**, *15*, 1445.
- (50) Mukherjee, R.; Gonuguntla, M.; Sharma, A. *J. Nanosci. Nanotechnol.* **2007**, *7*, 2069.
- (51) Kwon, S. J. *J. Appl. Phys.* **2006**, *99*, 063503.
- (52) Wei, J. H.; Coffey, D. C.; Ginger, D. *J. Phys. Chem. B* **2006**, *110*, 24324.
- (53) Baralia, G. G.; Filiatre, C.; Nysten, B.; Jones, A. M. *Adv. Mater.* **2007**, *19*, 4453.
- (54) Martin, C. P.; Blunt, M. O.; Pauliac-Vaujour, E.; Stannard, A.; Moriarty, P. *Phys. Rev. Lett.* **2007**, *99*, 116103.
- (55) Julthongpiput, D.; Zhang, W. H.; Douglas, J. F.; Karim, A.; Fasolka, M. J. *Soft Matter* **2007**, *3*, 613.
- (56) Berry, B. C.; Stafford, C. M.; Pandya, M.; Lucas, L. A.; Karim, A.; Fasolka, M. J. *Rev. Sci. Instrum.* **2007**, *78*, 072202.
- (57) Mukherjee, R.; Bandyopadhyay, D.; Sharma, A. *Soft Matter* **2008**, *4*, 2086.
- (58) Xuea, L.; Hana, Y. *Prog. Polym. Sci.* **2011**, *36*, 269.
- (59) Xu, L.; Reiter, G.; Shi, T. F.; An, L. J. *Langmuir* **2010**, *26*, 7270.
- (60) Schäffer, E.; Thurn-Albrecht, T.; Russell, T. P.; Steiner, U. *Nature (London)* **2000**, *403*, 874.
- (61) Deshpande, P.; Sun, X.; Chou, S. Y. *Appl. Phys. Lett.* **2001**, *79*, 1688.
- (62) Harkema, S.; Steiner, U. *Adv. Funct. Mat.* **2005**, *15*, 2016.
- (63) Voicu, N. E.; Harkema, S.; Steiner, U. *Adv. Funct. Mater.* **2006**, *16*, 926.
- (64) Wu, N.; Pease, L. F., III; Russel, W. B. *Adv. Funct. Mat.* **2006**, *16*, 1992.
- (65) Voicu, N. E.; Ludwigs, S.; Steiner, U. *Adv. Mater.* **2008**, *20*, 3022.
- (66) Wu, X. F.; Dzenis, Y. A. *J. Phys. D: Appl. Phys.* **2005**, *38* (16), 2848.
- (67) Herminghaus, S. *Phys. Rev. Lett.* **1999**, *83*, 2359.
- (68) Pease, L. F., III; Russel, W. B. *J. Chem. Phys.* **2003**, *118*, 3790.
- (69) Pease, L. F., III; Russel, W. B. *Langmuir* **2004**, *20*, 795.
- (70) Verma, R.; Sharma, A.; Kargupta, K.; Bhaumik, J. *Langmuir* **2005**, *21*, 3710.
- (71) Wu, N.; Russel, W. B. *Nano Today* **2009**, *4*, 180.
- (72) Kim, D.; Lu, W. *Phys. Rev. B* **2006**, *73*, 035206.
- (73) Tomar, G.; Shankar, V.; Sharma, A.; Biswas, G. *J. Non-Newtonian Fluid Mech.* **2007**, *143*, 120.
- (74) John, K.; Hänggi, P.; Thiele, U. *Soft Matter* **2008**, *4*, 1183.
- (75) Sarkar, J.; Sharma, A.; Shenoy, V. *Phys. Rev. E* **2008**, *77*, 031604.
- (76) Arun, N.; Sharma, A.; Pattader, P. S. G.; Banerjee, I.; Dixit, H. M.; Narayan, K. S. *Phys. Rev. Lett.* **2009**, *102*, 254502.
- (77) Srisvastava, S.; Reddy, P. D. S.; Wang, C.; Bandyopadhyay, D.; Sharma, A. *J. Chem. Phys.* **2010**, *132*, 174703.
- (78) Manigandana, S.; Majumder, S.; Suresh, A.; Ganguly, S.; Kargupta, K.; Banerjee, D. *Sens. Actuators, B* **2010**, *144*, 170.
- (79) Li, X.; Shao, J.; Ding, Y.; Tian, H.; Liu, H. *J. Micromech. Microeng.* **2011**, *21*, 115004.
- (80) Wu, N.; Kavousanakis, M. E.; Russel, W. B. *Phys. Rev. E* **2010**, *81*, 026306.
- (81) Lau, C. Y.; Russel, W. B. *Macromolecules* **2011**, *44*, 7746.
- (82) Kishore, V. A.; Bandyopadhyay, D. *J. Phys. Chem. C* **2012**, *116*, 6215.
- (83) Li, B.; Li, Y.; Xu, G.-K.; Feng, X.-Q. *J. Phys.: Condens. Matter* **2009**, *21*, 445006.
- (84) Lin, Z.; Kerle, T.; Baker, S. M.; Hoagland, D. A.; Schaffer, E.; Steiner, U.; Russell, T. P. *J. Chem. Phys.* **2001**, *114*, 2377.
- (85) Lin, Z.; Kerle, T.; Russell, T. P.; Schaffer, E.; Steiner, U. *Macromolecules* **2002**, *35*, 3971.
- (86) Lin, Z.; Kerle, T.; Russell, T. P.; Schaffer, E.; Steiner, U. *Macromolecules* **2002**, *35*, 6255.
- (87) Morariu, M. D.; Voicu, N. E.; Schäffer, E.; Lin, Z.; Russell, T. P.; Steiner, U. *Nat. Mater.* **2003**, *2*, 48.
- (88) Leach, K. A.; Gupta, S.; Dickey, M. D.; Wilson, C. G.; Russell, T. P. *Chaos* **2005**, *15*, 047506.
- (89) Dickey, M. D.; Gupta, S.; Leach, K. A.; Collister, E.; Wilson, C. G.; Russell, T. P. *Langmuir* **2006**, *22*, 4315.
- (90) Shankar, V.; Sharma, A. *J. Colloid Interface Sci.* **2004**, *274*, 294.
- (91) Craster, R. V.; Matar, O. K. *Phys. Fluids* **2005**, *17*, 032104.
- (92) Li, F.; Ozen, O.; Aubry, N.; Papageorgiou, D. T.; Petropoulos, P. G. *J. Fluid Mech.* **2007**, *583*, 347.
- (93) Roberts, S. A.; Kumar, S. *J. Fluid Mech.* **2009**, *631*, 255.
- (94) Bandyopadhyay, D.; Sharma, A.; Thiele, U.; Reddy, P. D. S. *Langmuir* **2009**, *25*, 9108.
- (95) Srisvastava, S.; Bandyopadhyay, D.; Sharma, A. *Langmuir* **2010**, *26*, 10943.
- (96) Reddy, P. D. S.; Bandyopadhyay, D.; Sharma, A. *J. Phys. Chem. C* **2010**, *114*, 21020.
- (97) Roberts, S. A.; Kumar, S. *Phys. Fluids* **2010**, *22*, 122102.
- (98) Atta, A.; Crawford, D. G.; Koch, C. R.; Bhattacharjee, S. *Langmuir* **2011**, *27*, 12472.
- (99) El-Sayed, M. F.; Moussa, M. H. M.; Hassan, A. A. A.; Hafez, N. M. *ISRN Appl. Math.* **2011**, *2011*, 498718-1–498718-35.
- (100) Amarandei, G.; Beltrame, P.; Clancy, I.; O'Dwyer, C.; Arshak, A.; Steiner, U.; Corcoran, D.; Theile, U. *Soft Matter* **2012**, *8*, 6333.
- (101) Oppenheimer, P. G.; Mahajan, S.; Steiner, U. *Adv. Optical Mater.* **2012**, *24*, 175.
- (102) Griffiths, D. J. *Introduction to Electrodynamics*; Prentice Hall of India Pvt. Ltd.: New Delhi, 1988.